J. Fluid Mech. (2021), *vol*. 921, A16, doi:10.1017/jfm.2021.486

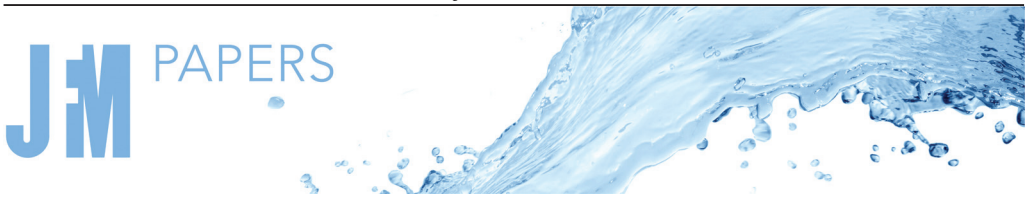

Particle radial distribution function and relative velocity measurement in turbulence at small particle-pair separations

Adam Hammond[1] **and Hui Meng**[1],†

[1]Department of Mechanical and Aerospace Engineering, University at Buffalo, Buffalo, NY 14260, USA

(Received 22 October 2020; revised 19 May 2021; accepted 26 May 2021)

Particle collisions in turbulent flow are critical to particle agglomeration and droplet coalescence. The collision kernel can be evaluated by radial distribution function (RDF) and radial relative velocity (RV) between particles at small separations r. Previously, the smallest r was limited to roughly the Kolmogorov length η due to particle position uncertainty and image overlap. We report a new approach to measuring RDF and RV near contact ($r/a \approx 2.07$, where a is particle radius). Three-dimensional particle tracking velocimetry using the four-pulse shake-the-box algorithm recorded short tracks with the interpolated midpoints registered as particle positions, avoiding image overlap and track mismatch. We measured RDF and RV of inertial particles in a one metre diameter isotropic air turbulence chamber with Taylor Reynolds number $Re_\lambda = 324$, $a = 12$–$16\ \mu\text{m}$ ($\approx 0.12\eta$) and Stokes number ≈ 0.7. At large r the measured RV agrees with the literature, but when $r < 20\eta$ the first moment of negative RV starts to increase, reaching 10 times higher values than direct numerical simulations of non-interacting particles. Likewise, RDF scales as $r^{-0.39}$ when $r > \eta$, reflecting the well-known scaling for polydisperse particles, but when $r \lessapprox \eta$, RDF scales as r^{-6}, yielding 1000 times higher near-contact RDF than simulations. Such RV enhancement and extreme clustering at small r can be attributed to particle–particle interactions including hydrodynamic interactions, which are not well-understood. Uncertainty analysis substantiates the observed trends. This first-ever simultaneous RDF and RV measurement at small separations provides a clear glimpse into the clustering and relative velocities of particles in turbulence near-contact.

Key words: particle/fluid flow, isotropic turbulence

† Email address for correspondence: huimeng@buffalo.edu

1. Introduction

Understanding the interaction of inertial particles dispersed in turbulence at close separations is critical to modelling particle collision rates. Turbulence drastically enhances the collision rates of water droplets in clouds (Shaw 2003), leading to a 'size gap' of particles with radii 10–50 μm (Ayala *et al.* 2008). Sundaram & Collins (1997) found that turbulence contributes to collision rates through particle preferential concentration and particle-pair RV

$$k(2a) = 4\pi(2a)^2 g(r)|_{r=2a} \langle w_r|_{r=2a}\rangle^-, \tag{1.1}$$

where $k(2a)$ is the collision kernel, r is the interparticle separation distance measured from centre-to-centre, a is the particle radius, $g(r)$ is the radial distribution function (RDF) and $w_r(r)$ is the particle-pair radial relative velocity (RV) and $\langle w_r|_{r=2a}\rangle^-$ is the first moment of the negative relative velocities, which will be referred to as 'inward RV' $\langle w_r|r\rangle^-$, evaluated at contact, expressed as $\int_{-\infty}^{0} w_r p(w_r|_{r=2a})\,\mathrm{d}w_r$, where $p(w_r|r)$ is the probability density function (p.d.f.) of RV at a given r.

These two collision-enhancing mechanisms by turbulence are strongly influenced by particle inertia measured by Stokes number St. For finite inertia, particles preferentially accumulate in the straining regions of the turbulent flow, enhancing the $g(r)$ at small r (Squires & Eaton 1991). Inertia also disrupts the correlation of motion between particles by ejecting particles from different energetic eddies and converging them in the straining region, thereby enhancing the inward RV, $\langle w_r|r\rangle^-$. This is known as the 'sling effect' (Falkovich, Fouxon & Stepanov 2002; Falkovich & Pumir 2007) verified experimentally by Bewley, Saw & Bodenschatz (2013), and also termed 'path-history effect' (Bragg & Collins 2014). Both of these mechanisms contribute to higher collision rates compared with inertia-free particles. Since they depend on particle–turbulence interactions (PTI), they are relevant to r scales down to approximately the Kolmogorov length η and below. When r decreases to $O(a)$, which is often $\ll \eta$, however, particle–particle interactions (PPI) become important. For example, hydrodynamic interactions (HI) arise through the disturbance of the flow field felt by one particle due to the presence of a nearby particle (Batchelor & Green 1972). Moreover, electrically charged particles will also experience attractive or repulsive Coulomb forces which can affect these collision statistics (Lu & Shaw 2015).

It is extremely difficult for direct numerical simulation (DNS) to simulate PPI in turbulence due to high computational expense (Ayala *et al.* 2014). Thus, simulations have been restricted to analysing the particle collision kernel contributed solely by PTI, called the geometric collision kernel (Ayala *et al.* 2008), wherein PPI are simply represented as a coefficient called the collision efficiency (Sundaram & Collins 1997; Brunk, Koch & Lion 1998) to be modelled theoretically (Wang *et al.* 2005) and estimated using DNS through implementation of these models (Wang *et al.* 2008). However, PPI may have complex influences on $g(r)$ and $\langle w_r|r\rangle^-$ at $r \lessapprox \eta$ that are not captured in a study of the geometric collision kernel.

In order to accurately calculate the collision kernel, it is imperative to capture both the effects of turbulence and PPI. Physical experiments offer the advantage of retaining these physics. However, experimental measurement of the collision rate (Bordás *et al.* 2013) has so far been limited to direct observation of liquid droplet coalescence, wherein it is difficult to discern the mechanisms leading to the observed collision rates. Improved methods with higher resolution (Kearney & Bewley 2020) could improve direct collision rate observation.

On the other hand, the collision kernel can be estimated by approaching (1.1) from the right-hand side, which nonetheless requires simultaneous RDF and RV measurements. Unfortunately, most experiments to date have lacked the spatiotemporal resolution to record particle motions at scales small enough to inform particle interactions. The first and perhaps only simultaneous experimental measurement of RDF and RV in isotropic turbulence known to us was by de Jong *et al.* (2010) using three-dimensional (3-D) digital holography. While the holographic lateral spatial resolution was adequate, the limited angular aperture of early digital holograms (Meng *et al.* 2004) caused excessive axial uncertainties (Cao *et al.* 2008). Furthermore, their two-pulse nearest neighbour particle tracking algorithm suffered severe tracking ambiguity and significant errors in RV calculations as r decreased (de Jong *et al.* 2010). Consequently they could not measure RDF and RV at $r \leqslant \eta$. However, their holographic RDF measurement (unaffected by tracking ambiguity) resulted in good comparison with DNS down to $r \approx \eta$ (Salazar *et al.* 2008).

Thereafter, more sophisticated tracking schemes have enabled improved RV measurements with resolution down to $r \approx \eta$. Saw *et al.* (2014) studied the scaling of RV at the dissipation scales of turbulence ($r \approx \eta$) using a time-resolved 3-D particle tracking velocimetry (PTV) technique with two-camera shadow imaging. Dou *et al.* (2018*a*) studied the dependence of RV on St and Taylor scale Reynolds number Re_λ in isotropic turbulence ($246 < Re_\lambda < 357$) using a four-frame planar PTV system, where the smallest separation was limited to $O(\eta)$ (Dou *et al.* 2018*b*). Meanwhile, recent RDF measurement has also overcome the $r \approx \eta$ resolution barrier. Yavuz *et al.* (2018) reported the first sub-Kolmogorov ($r/\eta \approx 0.2$) RDF measurement of particles in isotropic turbulence ($155 < Re_\lambda < 314$) by using a 3-D PTV technique to acquire particle positions. Their $g(r)$ clearly was drastically enhanced when $r \lessapprox \eta$, which was attributed to HI between particles. However, as r went below $O(10a)$, their $g(r)$ exhibited significant scatter, possibly due to insufficient resolution.

Here we report the first detailed, simultaneous measurement of RDF and RV down to near-contact, for estimation of the collision kernel with HI.

2. Challenges in measuring RDF and RV at small r

Measuring RDF and RV at small r down to near-contact requires minimizing particle position uncertainty and particle image overlap, two factors limiting the smallest measurable r. In non-holographic 3-D imaging, particle positioning uncertainty comes from two-dimensional (2-D) positioning uncertainties and errors in 3-D mapping from multiple cameras. Using iterative particle reconstruction (IPR) with the recently emerged multipulse shake-the-box (STB) algorithm brings particle position uncertainties down to 0.15 pixels (Novara *et al.* 2019), but when the pixel scale is small, this can be challenging to achieve if the experimental set-up experiences any slight vibrations.

The second factor limiting the smallest measurable r, particle image overlap, is an inherent hindrance to resolving particle pairs with small separations and more difficult to mitigate than the position uncertainties. Near-contact particles may overlap in their 2-D projections, leading to fused images that appear as single particles. This is exacerbated by optical diffraction of the high f-number lens for acquiring volumetric measurements, which enlarges the apparent particle image on the camera.

To avoid the particle image-overlap problem, we have devised a novel 3-D PTV technique using the four-pulse (4P) STB algorithm to accurately identify particle positions (and thus velocities) when particle separation r is small. We record successive particle

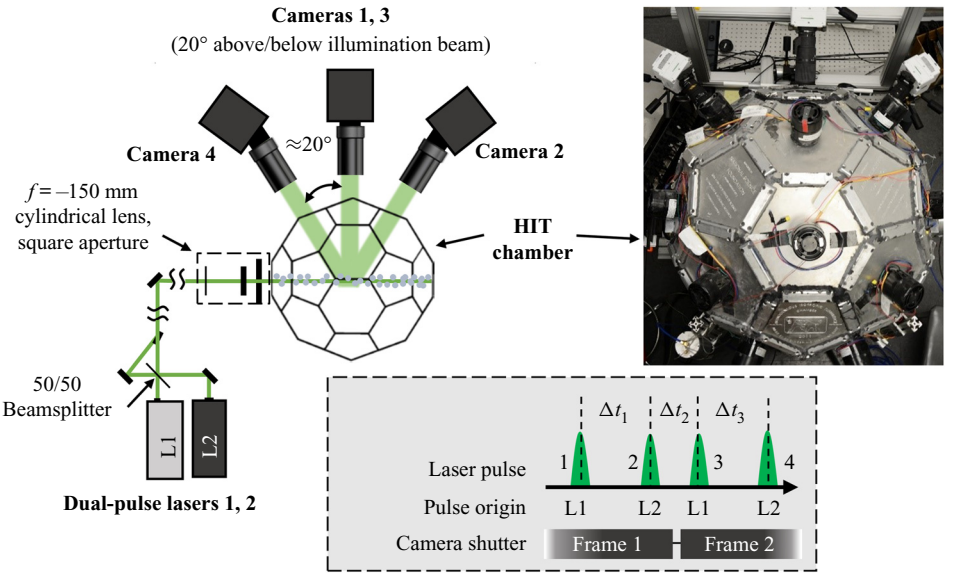

Figure 1. The 4P STB system (top view) and timing.

positions over a brief track of four instants and then identify particle position and velocity at the track midpoint for calculation of $g(r)$ and $w_r(r)$. When by chance the closest approach between two neighbouring particles is near the track midpoint, this strategy allows for acquisition of particle position without image overlap, thereby drastically reducing the smallest measurable r. In addition, the use of the midpoint of the 4P track further improves tracking accuracy by allowing the removal of mismatched particle identities (detailed in § 4). Our 4P tracking approach to mitigate the barrier of near-contact image overlap is the key to our ability to cast a first-ever glimpse into the near-contact particle positions and velocities in turbulent flows for collision statistic measurements.

3. Experimental set-up

3.1. *Isotropic turbulence flow facility*

We performed particle tracking in a high Reynolds number enclosed truncated icosahedron homogeneous isotropic turbulence (HIT) chamber (figure 1). This one metre 'soccer ball' shaped facility described in Dou *et al.* (2016) is a second-generation isotropic turbulence chamber, improved from the original cubic turbulence box (eight fans with Re_λ between 110 and 150) developed for our first attempt of simultaneous RDF and RV measurement (de Jong *et al.* 2010). The turbulence in the HIT chamber has been completely characterized in the central isotropic region (diameter 4.8 cm) by Dou *et al.* (2016). We held the fan speed constant such that $Re_\lambda = 324$ and used 3M K25 hollow glass spheres (3M, St. Paul, Minnesota) as particles, narrowing their diameter range to 25–32 μm using sieves, following the procedure in Dou *et al.* (2018*b*). The average density of the sieved particles was measured using a Micromeritics Accu-Pyc II 1340 gas-displacement pycnometer. The resulting particle and flow characteristics are listed in table 1.

To reduce complexity of our experiments, we kept the electric charge and gravity effects to a minimum. To minimize triboelectric charging of the particles caused by friction with the fans and walls, the inner surfaces of the turbulence chamber were coated in conductive

Particle type	3M K25 hollow glass microspheres
Particle radius	12.5 μm–16 μm
Stokes number	0.57–0.93
Average particle density	0.31 g cc^{-1}
Reynolds number Re_λ	324
Froude number Fr	13.4
Kolmogorov length η	123 μm
Kolmogorov time τ_k	1000 μs
Kolmogorov velocity v_k	0.13 m s^{-1}

Table 1. Particle and flow conditions. For complete details of turbulence in the HIT chamber see Dou *et al.* (2016).

carbon paint and electrically grounded, as described in Dou *et al.* (2018*b*). This helped to remove the charge on the particles. To mitigate the effect of gravity on the particles, we used fans as flow actuators in our chamber (Dou *et al.* 2016), which yielded a high Froude number $Fr = 13.4$. Furthermore, due to the low density and large size of our hollow glass spheres, the gravitational settling speed (assuming Stokes drag and a quiescent flow) of our particles was 0.007 m s^{-1}, compared with the Kolmogorov velocity of 0.13 m s^{-1}.

To prevent any transient effects in the statistics of particle motion due to particle injection, the particles were aerosolized, then pneumatically injected into the flow facility and allowed to equilibrate over 100 large eddy turnover times (≈30 s). The particle volume fraction was kept at $\sim 2.2 \times 10^{-5}$ (equivalent to 0.002 particles per pixel) to remain well within the dilute limit.

3.2. *Optical interrogation set-up*

3.2.1. *Optical configuration*

Figure 1 illustrates the 4P STB set-up for the HIT chamber. For each double-exposure double-frame recording, two dual-head Photonics Nd-YLF lasers (L1, L2) created a sequence of four independent 30 mJ laser pulses fired sequentially, to record the particles over four successive instants. To direct the pulses into an interrogation volume in the chamber centre, a series of optics combined the beams from both lasers to produce a single beam that spanned the chamber centre. A quarter-wave plate converted the cross-polarized laser beams to circular polarization for balanced particle scattering between pulses, and a concave cylindrical lens and square aperture sized the imaging volume as a 50 mm by 30 mm by 5 mm box. The illuminated particles were simultaneously captured by four identical high-speed cameras in frame-straddling mode (Phantom Veo 640L, 2560 by 1600 pixels, 200 mm macro lenses, $f/27$) positioned at different perspectives to triangulate the 3-D positions of particles. The cameras were positioned 20° from the normal direction of the laser sheet and oriented in a cross configuration (figure 1). The effective pixel scale was 21 μm. With a working distance of 0.7 m for the 0.5 m radius flow facility with a 0.2 m lens, it was critical to isolate for vibration, since miniscule incidental deviations of individual camera angles would lead to pixel-level deviation of pixel positions from the calibration.

3.2.2. *Vibration mitigation*

The four cameras were rigidly mounted on a passive vibration-isolating table, such that vibrations from external sources such as the turbulence chamber fan motors and building

vibration were damped. The table has a natural frequency of 3 Hz, so any undamped swaying motion of the table occurs over a time scale much larger than the 200 µs-duration recordings. Sways between recordings did not affect the statistics of r and w_r, since the sway was identical among the cameras, leading to translation of coordinate origin that is independent of $g(r)$ and w_r. To minimize breezes that might incidentally move lenses, the lasers were isolated from the cameras and laboratory ventilation was diverted during data collection.

3.3. *Implementation of STB particle tracking*

We implemented our small-r measurement strategy using the multipulse STB tracking algorithm (Novara *et al.* 2019; Sellappan, Alvi & Cattafesta 2020) based on STB (Schanz, Gesemann & Schröder 2016) implemented in DaVis 10.1 by LaVision GmbH (Göttingen, Germany), followed by an in-house particle-pair mismatch rejection code described in § 4. The STB particle tracking algorithm works by triangulating particle positions using an array of cameras and includes a unique approach to refine the particle position using the particle images, which makes it advantageous for small-r measurements. Important to our high-resolution measurements, the distance by which a particle is 'shaken' in each iteration (0.1 pixels in our experiments) plays into the resolution limit of STB, since it acts as a precision limit of the particle position. To minimize calibration error from small drifting of the camera and lens mounts, we performed the volume self-calibration with the images used to calculate RDF and RV. The final average disparity between self-calibration iterations was <0.1 voxel (≈2 µm), as recommended by Wieneke (2008).

The timing scheme is shown in figure 1. We chose $\Delta t_1 = \Delta t_3 = 1.6\Delta t_2$ based on the suggestion of $\Delta t_2 < \Delta t_{1,3}$ as a suitable choice for the recording of multiexposed images for STB (Novara *et al.* 2019; Sellappan *et al.* 2020), and based on minimizing Δt_2 to reduce uncertainty at small r due to interpolation error (see § 7). When $\Delta t_2 < \Delta t_{1,3}$, the tracking strategy is as follows. First, the particle images from the second and third pulse are tracked with a search area size based on the size of Δt_2. Based on the two-particle track, a search area is then placed centred around an extrapolation of the two-particle track to find the location of the particle at the times of pulses one and four. For complete detail on the tracking algorithm, refer to Sellappan *et al.* (2020). As recommended by LaVision, particle displacement should not be greater than 10 pixels to achieve a large dynamic range. Based on the root mean square velocity of the flow of 1.2 m s^{-1} (Dou *et al.* 2016), Δt_1 and Δt_3 were chosen to be 70 µs, and thus $\Delta t_2 = 44$ µs. To achieve statistical independence between recorded realizations, the repetition frequency of the four pulses was set at the lowest camera frame rate (12 Hz) such that the time between realizations was 83 ms, as compared with the large eddy turnover time of 150 ms (Dou *et al.* 2016).

The detailed values of the 4P STB inputs are as follows. The threshold for 2-D particle detection was 70 counts (out of 4096). This threshold was chosen as it was more than twice the noise threshold for the cameras. The maximum allowable triangulation error ϵ was 1.5 voxel (voxel size ≈ 21 µm), chosen as it yielded the largest number of resulting tracks among ϵ values in the range $0.8 < \epsilon < 2$. We used four iterations of the inner and outer shaking loops, the default for LaVision DaVis. Increasing the number of shaking loops did not appreciably change the number of recovered tracks. The shake length was 0.1 voxel, as it was below the particle position resolution (roughly 0.15 voxel) and default in LaVision DaVis. Particles were removed if found to have $r < 0.7$ voxel, as this condition was physically impossible for the particles in our experiments. In initial testing, multiple iterations of IPR produced no effect on the result, but drastically increased runtime. Therefore, during our measurements, only one iteration of IPR

was performed. In computation of the residuals in the STB algorithm, the particle size was not altered, but the intensity was increased by 20 % to prevent any chance of the same particle being tracked multiple times. To calculate the optical transfer function (OTF), the flow was divided into 50 equally sized subvolumes (5 by 5 by 2). For each subvolume and camera angle permutation (50 subvolumes by four cameras), a single OTF was generated to represent the particles in each subvolume, as seen by the camera. The original recorded particle images were then used to fit an OTF by finding the optimal values of weighting functions x_0, y_0, a, b and c as described in Schanz *et al.* (2012). The OTF is then used in 4P STB as detailed in Novara *et al.* (2019) and Sellappan *et al.* (2020).

Using the above described 4P STB technique, we recorded particle tracks in 15 465 realizations of the isotropic turbulent flow to ensure convergence of RDF and RV. The average and standard deviation of the number of analysed particles in each realization were 434 and 148, respectively. Each 4P track provides one instantaneous particle position and velocity. The particle positions and velocities were averaged over all realizations to calculate RV, followed by RDF.

Not all particles registered by the 4P STB algorithm were actually tracked due to its strict rejection of particles with fluctuating intensity to avoid particle misidentification. In the experiment, the laser beam path was over 6 m in order to isolate the laser cooling system from the flow facility to minimize incidental air gusts and vibration. This long laser beam path illuminated many ambient dust particles in the laboratory before reaching the turbulence chamber, causing fluctuation of illumination intensity inside the test volume. This causes the particle intensity to fluctuate from pulse to pulse, such that 62 % of particles were rejected by the 4P STB algorithm. By comparing the locations of tracked particles with untracked particles, we found untracked particles were dispersed evenly through the flow volume. This is expected, as motion of ambient dust is independent of the turbulence. Therefore, this track loss effectively results only in a reduction of particle number density and does not affect the RV or RDF, since changes in number density do not alter the RV and RDF. While estimating particle volume fraction, we have factored in this track loss. It should be noted that, for future experiments, inhomogeneity of laser illumination could be reduced by shortening the laser beam path, or by optical spatial filtering.

4. RV p.d.f.s calculation and results

4.1. *Radial RV calculation*

For particle A and B, their radial RV is defined as $w_r = (\boldsymbol{v_A} - \boldsymbol{v_B}) \cdot (\boldsymbol{r}/|\boldsymbol{r}|)$, where $\boldsymbol{v_i}$ is the velocity vector of particle i, and $\boldsymbol{r} = \boldsymbol{x_A} - \boldsymbol{x_B}$, where $\boldsymbol{x_i}$ is the position vector of particle i. For each realization of the turbulence, w_r of every particle pair in the flow was calculated. These w_r values were then binned by r for $2.07 < r/a < 650$ (equivalent to $0.24 < r/\eta < 81.1$) into 91 bins. The bins were logarithmically spaced and chosen to resolve the tails of p.d.f.s at the smallest separations. For each bin of r, we calculated the p.d.f. of w_r, $p(w_r(r))$. Figure 2 shows five representative p.d.f.s at $r/\eta = (0.24, 0.44, 0.92, 1.68, 10.2, 30.0)$, which correspond to $r/a = (2.07, 3.78, 7.91, 14.46, 88.4, 259)$.

4.2. *Removal of particle mismatch*

The particle number density used in this study is small (0.002 particles per pixel), such that, in general, particle tracking error is not expected to be prevalent.

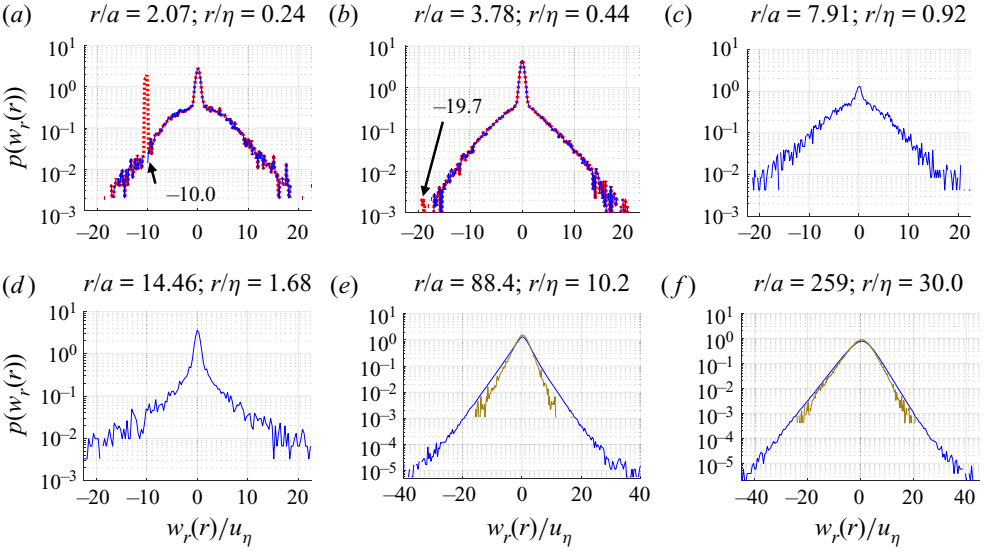

Figure 2. Probability density functions of particle-pair RV at six separations: (*a*) $r/a = 2.07$ (near contact), the prominent dashed-line peak was due to particle mismatches $w_{mis}/u_\eta = -10.0$ m s^{-1} correcting for mismatch results in the blue curve; (*b*) $r/a = 3.78$, the peak due to mismatches diminished; (*c*) $r/a = 7.91$; (*d*) $r/a = 14.46$; (*e*) $r/\eta = 10.2$ compared with Dou *et al.* (2018*a*); (*f*) $r/\eta = 30.0$, compared with Dou *et al.* (2018*a*), with more prominent negative skewness. The red dotted line is for before mismatch removal (current study), the blue solid line is for after mismatch removal (current study) and the tan solid line is for Dou *et al.* (2018*a*).

For small-number-density cases, tracking ambiguity may still occur when pairs of particles are extremely near to one another. The result of this tracking ambiguity is that, although rare, the tracking algorithm may swap the identity of the tracked particle with its neighbour, leading to erroneously crossed particle tracks. We term this track-swapping phenomenon as 'mismatch'. When tracks erroneously cross, the apparent particle separation at the crossing is extremely small. If this swap occurs between pulses two and three, this will lead to an erroneous, near-contact separation at the track midpoint. Because of the swap, there will also be a false inward RV from the false 'relative velocity' from the pairs switching places. When this occurs, the RV will appear as $w_{mis} = (-2r_{mis})/\Delta t_2$. This expression comes directly from the tracking algorithm switching the particle positions: a false inward displacement of the particles ($-2r_{mis}$) has been manufactured over the track interpolation time (Δt_2) by the tracking algorithm.

We use w_{mis} to identify and remove mismatched tracks. The first pass of $p(w_r(r))$ calculation is shown in figure 2(*a*,*b*) as the red dashed curves. The sharp spike at -1.34 m s^{-1} for $r/a = 2.07$ in figure 2(*a*) was exactly w_{mis}. After removing particles with $w_r = w_{mis}$ from each p.d.f., we obtained the corrected RV p.d.f.s for all the conditions, exemplified by the blue curves in figure 2. For $r/a \gtrapprox 3.78$, w_{mis} was beyond the maximum measurable w_r based on the dynamic range of the velocimetry system and, therefore, its removal was inconsequential.

4.3. *RV p.d.f. result discussion*

As exemplified by figures 2(*a*) and 2(*b*), all the RV p.d.f.s for $r/\eta \lessapprox 0.5$ exhibit a prominent narrow core abruptly transitioning to broad tails. This suggests that there could

be two additive mechanisms driving the particle RV at small separations. In contrast, as demonstrated in figures 2(*e*) and 2(*f*) ($r/\eta = 10.2$ and $r/\eta = 30.0$), the p.d.f.s at very large separations do not exhibit a core-and-tail structure, though there is a slight upturn visible at the most extreme values of $w_r(r)$. Starting from near-contact, when r/η increases to ≈ 0.5, the core remains qualitatively the same, but the curvature of the tails decreases (see figure 2*a*,*b*). As r/η further increases to approximately unity, the core becomes obscured by the rise of the tails (see figure 2*c*). As r/η continues to increase beyond unity, the tails drop lower, revealing a structurally different core with smooth transitions to the tails. With further increase of r/η, the tails diminish, leaving the linear-in-the-logarithm-scale core to widen (see figure 2*e*,*f*).

To compare our RV results against the literature, in figures 2(*e*) and 2(*f*) we coplot our results with the RV p.d.f. from the experimental measurement by Dou *et al.* (2018*a*) under the same flow and particle conditions and thus the same St and Re_λ as in the current study. However, Dou *et al.* (2018*a*) used a different, 2-D particle tracking technique. Both p.d.f.s show a linear core shape in the logarithm scale, but that by Dou *et al.* (2018*a*) was narrower. This is likely due to their 2-D technique (as opposed to our 3-D technique), which led to underprediction by $\sqrt{2/3}$.

In figures 2(*e*) and 2(*f*), we observe the RV p.d.f.s to be slightly negatively skewed. This is expected as a result of vortex stretching in turbulence (Tavoularis, Bennett & Corrsin 1978). In smaller separations (figure 2*a–d*) the p.d.f.s become symmetric. Compared with the RV p.d.f.s of Saw *et al.* (2014) who did observe skewness in their RV p.d.f.s at $r/\eta \approx 1$, the tails of our RV p.d.f.s are much higher. This means that we observed larger RV values more frequently than they did in their experiments, which may have overshadowed the less-frequent negative skewness effects caused by vortex stretching. It should be noted that our experiments were under very different conditions (e.g. larger a, smaller density ρ, smaller η, solid particles) compared with those of Saw *et al.* (2014). These different conditions could have caused PPI to occur at larger r/η in our experiments than in Saw *et al.* (2014).

4.4. *Inward RV result*

For the collision kernel in (1.1), we calculated the first moment of negative velocities $\langle w_r|r\rangle^- = \int_{-\infty}^0 w_r p(w_r|r)\,\mathrm{d}w_r$ and plotted it against r/η and r/a in figure 3 (vertical bars), along with experimental results by Dou *et al.* (2018*a*) (triangles) and DNS results by Ireland, Bragg & Collins (2016) (solid line). The vertical error bars in the new experimental results were calculated as described in § 7: uncertainty by tracking input sensitivity. As r/η decreases from 80 to 3 (denoted as region I), our measured $\langle w_r|r\rangle^-$ decreases monotonically, consistent with previous results. However, at $r/\eta = 3$ ($r/a = 25$), the newly measured $\langle w_r|r\rangle^-$ turns upward with decreasing r. When $r/\eta \sim 1$ it plateaus. After $r/\eta \sim 0.6$ it decreases again, reaching a minimum at $r/\eta = 0.4$. We denote this region, $0.4 < r/\eta < 3$ (which corresponds to $3.3 < r/a < 25.9$) as region II. When r decreases further towards contact, $\langle w_r|r\rangle^-$ increases again, reaching approximately $1.2u_\eta$ at $r/a = 2.07$. This is denoted as region III. The shaded regions around our measurement data represent horizontal uncertainties arising from track interpolation (detailed in § 7). Note that the DNS by Ireland *et al.* (2016) assumed one-way coupling (no PPI) for monodisperse inertial particles at $St = 0.7$ and $Re_\lambda = 398$.

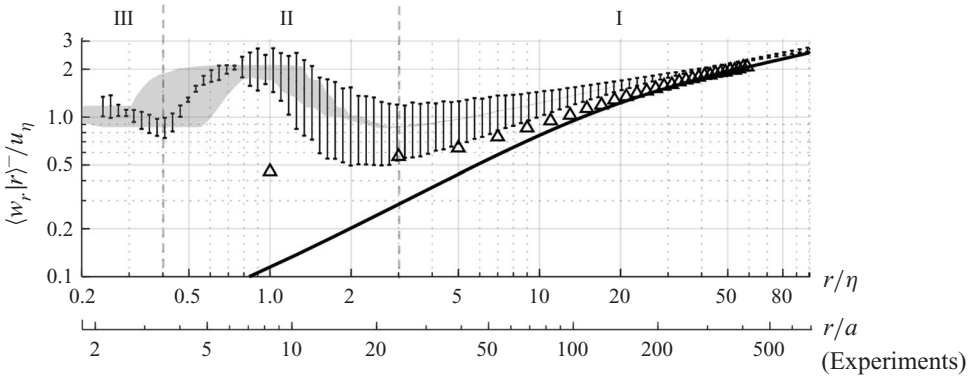

Figure 3. Plot of $\langle w_r|r\rangle^-$ normalized by u_η, compared with Dou *et al.* (2018*a*) and DNS of Ireland *et al.* (2016). The shaded region represents the uncertainty due to interpolation, interpreted as the range of r which may contribute to the measurement. The vertical error bars are calculated as in § 7, uncertainty by tracking input sensitivity. From the right, regions I, II and III are characterized by the monotonic decrease due to turbulence, a plateau and an increase towards contact, respectively. The vertical bars are the current study, the triangles are the experiment by Dou *et al.* (2018*a*) and the solid curve is the DNS by Ireland *et al.* (2016).

4.5. *Inward RV result discussion*

Figure 3 shows that at very large r in region I, all results overlap. At these scales, turbulence alone drives the particle relative motion. As such, the DNS of non-interacting particles match the experiments. As r decreases to $r/\eta = 20$ in region I, both experimental studies show higher $\langle w_r|r\rangle^-$ than the DNS. This could be due to the presence of weak PPI, which is not accounted for in the DNS. Between the two experiments, the results of this study are higher than those of Dou *et al.* (2018*a*), due to differences between the 3-D and 2-D measurements. Dou *et al.* (2018*a*) speculated particle polydispersity in their experiments as the cause for their elevated $\langle w_r|r\rangle^-$ compared with DNS. However, we believe that polydispersity effects are not dominant until r decreases to region III.

Starting in region II ($r/a \approx 25$), the inward RV begins to increase, indicating a decorrelation of the particle relative motion. Qualitatively, the increase of $\langle w_r|r\rangle^-$ is reminiscent of inward drift by HI between inertia-free particles (Brunk, Koch & Lion 1997). However, since our particles have appreciable inertia, the interactions between them may be more complicated than the HI predicted for inertia-free particles by Brunk *et al.* (1997). The measured inward RV then peaks at around $r/a \approx 10$ and decreases thereafter. Brunk *et al.* (1997) explained that lubrication suppresses the RV between particles. Their theory predicted a peak at $r/a \approx 2.08$, however, our data peaks at $r/a \approx 10$. If the peak and downturn we observed was from lubrication, this would mean that lubrication is acting across longer distances than the prediction by Brunk *et al.* (1997).

In region III, $\langle w_r|r\rangle^-$ is enhanced again, which we believe is an effect of polydispersity on the particle motion in the flow. Particles of different sizes will respond to the flow differently, thus enhancing their relative velocities. Although we aimed to produce monodisperse particles by sieving (as described in Dou *et al.* (2018*b*)), the sieved particles have a narrow but finite size distribution. When r decreases to the scales of multiple radii, the minute difference in particle size will lead to the enhancement of RV. Relative velocity enhancement due to dispersion of particle size has been previously observed in simulations of bidisperse, non-interacting particles (Zhou, Wexler & Wang 2001).

5. RDF calculation and results

5.1. *RDF calculation*

The RDF measures the degree of particle clustering in the flow. It compares the expected number of satellite particles at a distance r from each primary particle with the number of expected satellite particles in a uniform spatial distribution. It can be calculated by binning the particle pairs according to their separation distance, and then calculating (Salazar *et al.* 2008) $g(r_i) = N_i/(\Delta V_i)/N/V$, where N_i is the number of particle pairs separated by a distance of $r_i \pm \Delta r/2$ and Δr is the width between the bins. Here ΔV_i is the volume of a spherical shell of radius r_i and thickness Δr, N is the total number of particle pairs and V is the overall volume of the flow. Using this approach, we calculated the RDF for each of the 15 465 realizations, then took the ensemble average of all the RDFs as the result.

5.2. *RDF boundary treatment*

When RDF is calculated in a finite sample volume, it is paramount to properly treat the boundary to obtain accurate estimation of $g(r)$ at large r. Without it, those primary particles near the edge would not have satellite particles to pair with in space outside the imaging volume. This would lead to an underestimation of N_i that affects more particles as r increases, leading to diminishment in $g(r)$ which intensifies as r increases.

A recent study by Larsen & Shaw (2018) discussed the boundary treatment for RDF in depth, outlining two methods suitable for RDF experiments: the guard area approach, which allows the user to define the volume within a distance δx from the boundary edges wherein particles may only be considered as satellites for pairing; and their new effective volume approach, which accounts for the edge-effects of primary particles near the volume boundary and does not exclude these particles. The former is computationally inexpensive but loses data, while the latter retains data for statistical convergence but is computationally expensive when used at high resolution. For our boundary treatment in RDF calculations, we combined these two strategies: we used a $\delta x = 0.5$ mm guard area for $0 < r \leqslant 0.5$ mm and the effective volume approach for $r > 0.5$ mm.

5.3. *RDF result*

Using the particle position data from the particle tracks, we calculated the RDF using boundary treatment. The resulting RDF is plotted in figure 4. To visualize the scaling from large r down to $r \approx \eta$, in figure 4(*a*), $g(r)$ is plotted against r/η. Furthermore, to examine $g(r)$ at small separations down to contact, in figure 4(*b*), we replot $g(r)$ against r/a for $2.07 < r/a < 35$, which corresponds with $0.23 \leqslant r/\eta \leqslant 0.4$. The shaded region on $g(r)$ represents the error bounds of r, which reflect the interpolation effect on the measurements, as detailed in § 7. The vertical error bars are uncertainty by tracking input sensitivity calculated in § 7.

The entire regime of r can be divided into regions I, II and III consistent with the RV plot (figure 3). In large scales (figure 4*a*), $g(r) \to 1$ as $r/\eta \to \infty$, as expected in isotropic flows. As r decreases across region I and a part of region II, the RDF increases by a well known power law scaling $g(r) \propto r^{-c_1}$, evidently due to the preferential concentration effect (Reade & Collins 2000). As r further decreases to $r/a \approx 12$, which is $r/\eta \approx 1.5$, the RDF starts to exhibit a surprising explosive increase. As r goes below $r/a \approx 3.5$ (region III), the RDF plateaus.

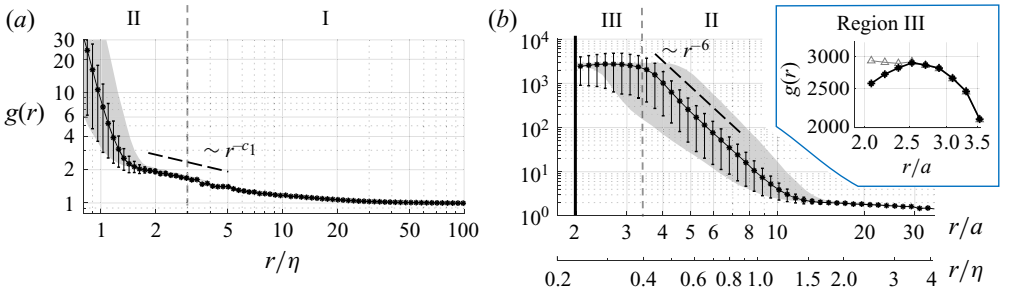

Figure 4. Measured RDF of particles in isotropic turbulence ($St = 0.74$, $Re_\lambda = 324$). The shaded area represents the uncertainty in r from interpolation uncertainty, i.e. the range of r which may contribute to the measurement. The vertical error bars are uncertainty by tracking input sensitivity calculated in § 7. (*a*) Plot of $g(r)$ against r/η in the range $0.8 \leqslant r/\eta \leqslant 100$. (*b*) Plot of $g(r)$ against r/a in the range $2.07 \leqslant r/a \leqslant 34$, where the solid vertical line represents contact. Regions I, II and III are separated by dashed vertical lines. The insert shows the effect of mismatch removal in region III, near contact. The grey triangles represent $g(r)$ before mismatch removal and the black asterisks represent $g(r)$ after mismatch removal. All axes are logarithm scaled.

5.4. *Effects of mismatch removal*

Particle mismatch over the track midpoint not only caused a spurious spike in RV p.d.f. as shown earlier, but also artificially increased RDF at near-contact r. The inset of figure 4(*b*) shows that particle mismatch occurred at $r/a < 2.75$, and mismatch removal led to a 20 % correction (reduction) in the near-contact RDF. For $r/a \gtrapprox 2.75$, mismatch removal made no difference to the RDF estimates.

5.5. *RDF result discussion*

A power law fit of the r^{-c_1} regime observed in the RDF yielded $c_1 = 0.39$, which is smaller than $c_1 = 0.69$ reported by DNS from Ireland *et al.* (2016) for monodisperse particles at $St = 0.7$. Our measured c_1 value is reasonable, since the particles in the experiments are polydisperse, and polydispersity diminishes the value of c_1 for the overall particle sample based on the least clustered particle population (Saw *et al.* 2012*a*,*b*). In our experiment, the least clustered population is comprised of the smallest St particles in the sample. To properly compare the experimental c_1 against DNS, simulations would need to use the same particle radius distribution as in the experiment.

Theoretical models of far-field particle–particle HI of inertia-free particles show that the pair probability $\rho(r)$, which is proportional to $g(r)$, scales with r^{-6} (Brunk *et al.* 1997). This scaling arises by solving their (28) using the far-field forms of their functions. In figure 4(*b*) we observe a clear r^{-6} scaling in $g(r)$. This suggests that HI may be dominating RDF in region II in our experiments, even though Brunk *et al.* (1997) predicted r^{-6} scaling for inertia-free particles. Incidentally, Yavuz *et al.* (2018) reported a strong upturn in $g(r)$ near $r/a \approx 10$ similar to our experiment, but did not report any r^{-6} scaling. Instead, they used theoretical analyses to infer that the r^{-6} scaling regime would have occurred at a smaller r than their experiment could resolve. We hold the opinion that their data in these small separations could well have embedded r^{-6} scaling, except that it was obscured by their experimental noise evidenced by the large scatter of their data.

At the start of region III ($r/a \lessapprox 3.3$), $g(r)$ starts to plateau. This is likely due to particle polydispersity discussed above for inward RV in the same region. The DNS of non-interacting particles have shown that polydispersity diminishes the turbulence enhancement of $g(r)$, leading to $g(r)$ plateauing at small r (Saw *et al.* 2012*a*,*b*; Dhariwal

& Bragg 2018). Similarly, we suspect that polydispersity also diminishes the PPI enhancement of $g(r)$, albeit at even smaller r. In both cases, the effect of polydispersity is to decorrelate particle responses to the local flow. For turbulence, this decorrelation arises due to the varying levels of inertia of the particles (Saw *et al.* 2012*a*). For PPI such as HI, we suspect that this decorrelation arises due to the varying sizes of the particles.

6. Enhancement of RV, RDF and collision kernel

6.1. *RV enhancement*

Figure 3 shows that as r decreased, our experimentally measured inward RV $\langle w_r(r)|r\rangle^-$ turned upward at the border between regions I and II, instead of continuing the monotonic decrease predicted by the DNS (Ireland *et al.* 2016). Other DNS studies also predicted similar monotonic decreases (Wang *et al.* 2008; Rosa *et al.* 2013), even when including a quasi-steady Stokes flow model for HI (termed aerodynamic interactions in their reports). Wang *et al.* (2008) reported that the addition of HI marginally weakened the inward RV and did not change its monotonic decrease as r decreased. Our experimental measurement of inward RV in region II shows a more complex behaviour. Since our experiment does not use simplifying assumptions and captures the full physics over the range that the experiment can resolve, we conjecture that previous simulations did not fully account for particle interactions.

6.2. *RDF enhancement*

At r/a=12 (or $r/\eta = 1.5$), the RDF value is still comparable to previous experiments and DNS results by Salazar *et al.* (2008), but the immediately following $g(r)$ enhancement by PPI that scales as r^{-6} brings RDF all the way to a staggering 2000 at $r/a = 3.5$. The near-contact $g(r)$ is thus $O(10^3)$, compared with extrapolation from the r^{-c_1} scaling from PTI alone, which was $O(10)$. Prior DNS without HI (Wang, Wexler & Zhou 2000; Ireland *et al.* 2016) and with a model for HI (Wang *et al.* 2008; Rosa *et al.* 2013) also predicted a power law scaling exponent that leads to a near-contact $g(r)$ of $O(10)$. This suggests that our experimental data may contain physics not captured by prior models.

6.3. *Collision kernel*

From our near-contact RDF and RV data, a collision kernel that retains PPI (HI included, in absence of the Coulomb force) can be calculated. To compare with DNS, we calculated the non-dimensional collision kernel $\hat{k}(2a) = k(2a)/(2a)^2 u_\eta$ following Ireland *et al.* (2016). From the smallest measured separation $r/a = 2.07$, we extrapolate RDF and RV down to $r/a = 2.00$, obtaining $g(r)|_{r=2a} = 2500$ and $\langle w_r|r = 2a\rangle^- = 1.2$ m s^{-1} at contact. This yields $\hat{k}(2a) = 2.9 \times 10^5$ for $St \approx 0.75$, $a \approx 14$ μm, $Re_\lambda = 324$. Since RDF is enhanced far more than RV, it is evident that PPI enhances the collision rate mostly through increasing clustering.

While our measurement resolution allowed for probing the statistics at very small separations (down to $r/a = 2.07$), the measured r is subject to interpolation uncertainty in particle tracking (§ 7). This uncertainty in r will affect the statistics of $g(r)$ and $\langle w_r|r\rangle^-$, which depend on r. Consequently, effects of physics that drive particle RV or RDF will be averaged over the r uncertainty, which could be wider than the relevant r of the physics itself. For example, the breakdown of the fluid continuum assumption occurs at separations of the order of the mean free path in air, which is much less than $r/a = 2.07$. The masking of this effect could lead to error in the extrapolation to contact

for calculation of the collision kernel. Indeed, to to accurately estimate the collision kernel at contact, all near-contact physics need to be accounted for, which is beyond the current experimental capabilities. However, our experiments have already pushed the envelope for future modelling by providing collision statistics at much closer-to-contact separations, allowing collision kernel estimations that are more credible than extrapolation from the PTI-dominated regime (region I).

Our calculated collision kernel is four to six orders of magnitude higher than DNS predictions by Ayala *et al.* (2008) and Ireland *et al.* (2016) under the one-way coupling assumption and neglecting PPI, which are $\hat{k}(2a) = 0.1$–10 for $St \approx 0.1$–1.0 and $Re_\lambda =$ 88–597. This astounding collision enhancement provides experimental evidence that PPI drastically increase particle collision rates. Evidently, prior models of HI implemented in simulations did not fully capture the extent of the enhancement of collision rates as observed in this experiment. As mentioned above, simulations with prior HI models (e.g. Wang *et al.* 2008) obtained results that were functionally similar to the DNS results without any PPI, with only slight magnitude differences. Thus, the models of PPI used in the past for simulating collision statistics in turbulent flows may not fully reflect the true nature of particle interactions at near-contact separations.

7. Measurement uncertainty

7.1. *Sample size and statistical convergence*

To ensure that the experimental results were statistically significant, we aimed to acquire sufficient experimental data to converge the RV and RDF statistics with minimal standard error. The data was taken over 15 465 realizations, with on average 434 particles per frame. The sample size of particle pairs in a given bin of separation for calculation of the RV and RDF ranged from $O(10^3)$ to $O(10^6)$. In figure 5 we plot the relative uncertainty based on the standard error of the mean for both inward RV and RDF along with the sample size at select r bins. We find that for both statistics, the relative standard error always remains below 5 %. The highest relative standard error occurs not at r near contact, but in region II, where the sample size is also the lowest. This corresponds to the beginning of the r^{-6} upturn in RDF, and the regime where inward RV increases for decreasing r. Due to the clustering, there are fewer particle pairs at these intermediate separations.

7.2. *Sample size of the removed mismatches*

To ensure that the complete removal of the mismatches (described in § 4) did not affect the RV and RDF statistics, we compared the number of mismatches with the total sample size. There were a total of 8277 mismatched particle pairs out of 1.19×10^9 total particle pair samples and 97 % of the mismatched particle pairs were found across the first five bins. The percentage of mismatches dropped quickly from 15 % (first bin, $r/a = 2.07$) to 0.3 % (fifth bin, $r/a = 2.70$). The removal of these mismatches did not affect the RV and RDF in these bins because the true separations of the mismatches were larger than r_{mis} (see 4, removal of particle mismatch). The bins belonging to the true separations of these particles have orders of magnitude more data than even the total number of mismatches, and thus removal of these mismatches are inconsequential.

7.3. *Interpolation uncertainty*

Our track interpolation technique allowed us to obtain $w_r(r)$ and $g(r)$ at much smaller r than previously possible. However, the accuracy of r and $w(r)$ at the track midpoint

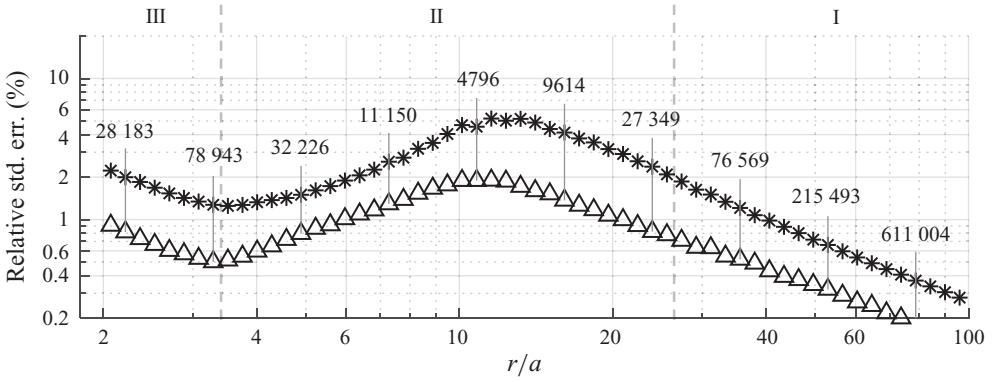

Figure 5. Relative standard error of the mean for inward RV (asterisks) and RDF (triangles) as a function of separation. The dashed vertical lines separate regions I to III. The numbers above the vertical-line-marked symbols correspond to the total number of recorded particle pairs for the marked bin. The number of counts per bin increases as r/a increases beyond 100. The total number of particle pairs for the entire experiment was 1.19×10^9.

is still limited by the spatiotemporal resolution of the experimental set-up. Despite the interpolation time Δt_2 being small, it is still finite. Since there is a relative velocity between particles, the instantaneous value of r varies over the interpolation time Δt_2. This means there is uncertainty in the true r at the time of track midpoint due to the interpolation. In other words, if particle pairs have fluctuations in their relative position over the track that occur over time scales smaller than Δt_2, the particle track recovered by 4P STB will not reflect these fluctuations.

To quantify this interpolation uncertainty, we calculated the root mean square radial distance travelled by particles between the second and third pulse of the 4P track as $\delta r_{in} = \Delta t_2 \sqrt{\langle w_r^2(r) \rangle}$, where $\langle w_r^2(r) \rangle$ is the variance of the particle-pair radial RV p.d.f. This affords an estimate of the range of r values, with potentially different physics, that may contribute to the data used to calculate RDF and RV at a given r bin. When δr_{in} becomes comparable with r, the interpolation uncertainty must be considered to interpret the results.

7.4. *Confidence interval based on interpolation uncertainty*

To account for the effect of interpolation over r, a confidence interval $r \pm \delta r_{in}$ is added as the shaded regions (consisting of horizontal bars) in $g(r)$ and $\langle w_r|r \rangle^-$ in figures 3 and 4. Clearly, interpolation uncertainties are negligible at large r, but as r decreases to the order of η, the confidence intervals start to widen.

A question then arises as to whether the upward and downward trends of these curves are real. Note that in figure 3, even at contact, particle pairs cannot be misconstrued as pairs separated by $r/a \approx 4$ with the same value of $\langle w_r|r \rangle^-$, since the confidence intervals at $r/a \approx 4$ do not reach as far as $r/a = 2$ (contact), and *vice versa*. Likewise, in figure 4, the r^{-6} scaling of $g(r)$ and the r values for the plateau are significant. Hence, we believe that all the observable trends in $g(r)$ and $\langle w_r|r \rangle^-$ are real. However, when the particles are nearly in contact, the relevant time scale of particle interaction τ_x should diminish, and the physics dominating time scales $\tau_x < \Delta t_2$ is not captured. This may include lubrication forces, which dampen relative velocities extremely near to contact, i.e. when $r/a \approx 2.08$ for inertia-free particles (Brunk *et al.* 1997). This is a current limitation of our technique.

7.5. *Particle position uncertainty*

The recorded particle positions from the tracks themselves have uncertainties, which affect the precision of r and thus $w_r(r)$ and $g(r)$. Owing to our careful measures to acquire high-quality tracks through vibration isolation and volume self-calibration on the images used to collect data, we expect that our position uncertainty is on a par with 0.15 pixels (Novara *et al.* 2019), which, based on a camera pixel size of 21 μm, translates into a position uncertainty $\delta x = 3.2$ μm and an r uncertainty of $\delta r = \sqrt{2}(0.15)(21\ \mu\text{m}) \approx 4.5$ μm estimated via propagation (Moffat 1988). These uncertainties, only a fraction of the particle radius, are overshadowed by the interpolation uncertainty.

7.6. *Uncertainty by tracking input sensitivity*

The 4P STB particle tracking algorithm has many user-defined parameters. Among these, the allowable triangulation error ϵ is considered the most important and consequential parameter affecting the output (Novara *et al.* 2019). We used $\epsilon = 1.5$ voxel (1 voxel $\approx$ 21 μm), since this value produced the most total tracks when tested against nearby values. To test the sensitivity of RV and RDF to variation in ϵ, thereby acquiring an estimation of vertical error bars, we varied ϵ by $\pm 10\,\%$ and calculated inward RV and RDF at $\epsilon = 1.35$ and 1.65 voxels. For each separation, we then took twice the standard deviation of the results ($\epsilon = 1.35$, 1.5 and 1.65 voxels) as the vertical error bar for the inward RV and RDF, shown in figures 3 and 4. This process is akin to 'ensemble forecasting' in weather prediction, where multiple different forecasts are produced with different input conditions to estimate the range of potential weather outcomes.

The resulting error bars show that at near-contact the RV was not strongly affected by the triangulation error. At this separation, the vertical error bar from the uncertainty by tracking input sensitivity was 14 %, a few times the standard error (2.3 %). On the other hand, for the RDF uncertainty at near-contact, there is potential for 60 % variation in the experimental result of RDF, even though the standard error is 1 %. However, this variation does not change the order of magnitude of the predicted RDF.

8. Conclusions

We report the first-ever detailed, simultaneous measurement of RDF and RV at much smaller r down to near-contact for experimental estimation of the collision kernel. Based on a 4P STB particle tracking technique, our novel track-midpoint particle positioning approach aided by a mismatch rejection algorithm has allowed acquisition of particle positions at much smaller r than previously possible, leading to observations of dramatic enhancements of inward RV and RDF. The data reveal three distinct regions of particle separation distance: PTI-dominated region I (down to $r/\eta = 3$); PPI-dominated region II ($0.4 < r/\eta < 3$), containing three inversions in $\langle w_r|r\rangle^-$ and r^{-6} scaling in $g(r)$; PPI-dominated region III, where $\langle w_r|r\rangle^-$ increases and $g(r)$ plateaus due to polydispersity. The resulting non-dimensional collision kernel is four to six orders of magnitude higher than predictions by DNS, which do not model PPI. We hope that the new experimental data from this study will stimulate more investigations of near-contact physics and thereby help improve modelling of particle collision statistics accounting for PPI.

Acknowledgements. We are grateful to A.D. Bragg for stimulating discussions and critique, D. Johnson for editorial assistance as well as L. Collins and R. Shaw for helpful discussions.

Funding. We thank the National Science Foundation for support through the Major Research Instrumentation program (award 1828544, program manager H. Chelliah). We thank LaVision for their continuous technical support.

Declaration of interests. The authors report no conflict of interest.

References

Ayala, O., Rosa, B., Wang, L.-P. & Grabowski, W.W. 2008 Effects of turbulence on the geometric collision rate of sedimenting droplets. Part 1. Results from direct numerical simulation. *New J. Phys.* **10** (7), 075015.

Ayala, O., Parishani, H., Chen, L., Rosa, B. & Wang, L.-P. 2014 DNS of hydrodynamically interacting droplets in turbulent clouds: parallel implementation and scalability analysis using 2D domain decomposition. *Comput. Phys. Commun.* **185** (12), 3269–3290.

Batchelor, G. & Green, J.-T. 1972 The hydrodynamic interaction of two small freely-moving spheres in a linear flow field. *J. Fluid Mech.* **56** (2), 375–400.

Bewley, G.P., Saw, E.-W. & Bodenschatz, E. 2013 Observation of the sling effect. *New J. Phys.* **15** (8), 083051.

Bordás, R., Roloff, C., Thévenin, D. & Shaw, R. 2013 Experimental determination of droplet collision rates in turbulence. *New J. Phys.* **15** (4), 045010.

Bragg, A.D. & Collins, L.R. 2014 New insights from comparing statistical theories for inertial particles in turbulence: II. Relative velocities. *New J. Phys.* **16**, 055014.

Brunk, B.K., Koch, D.L. & Lion, L.W. 1997 Hydrodynamic pair diffusion in isotropic random velocity fields with application to turbulent coagulation. *Phys. Fluids* **9** (9), 2670–2691.

Brunk, B.K., Koch, D.L. & Lion, L.W. 1998 Turbulent coagulation of colloidal particles. *J. Fluid Mech.* **364**, 81–113.

Cao, L., Pan, G., de Jong, J., Woodward, S. & Meng, H. 2008 Hybrid digital holographic imaging system for three-dimensional dense particle field measurement. *Appl. Opt.* **47** (25), 4501–4508.

Dhariwal, R. & Bragg, A.D. 2018 Small-scale dynamics of settling, bidisperse particles in turbulence. *J. Fluid Mech.* **839**, 594–620.

Dou, Z., Bragg, A.D., Hammond, A.L., Liang, Z., Collins, L.R. & Meng, H. 2018*a* Effects of Reynolds number and Stokes number on particle-pair relative velocity in isotropic turbulence: a systematic experimental study. *J. Fluid Mech.* **839**, 271–292.

Dou, Z., Ireland, P.J., Bragg, A.D., Liang, Z., Collins, L.R. & Meng, H. 2018*b* Particle-pair relative velocity measurement in high-Reynolds-number homogeneous and isotropic turbulence using 4-frame particle tracking velocimetry. *Exp. Fluids* **59** (2), 30.

Dou, Z.W., Pecenak, Z.K., Cao, L.J., Woodward, S.H., Liang, Z. & Meng, H. 2016 PIV measurement of high-Reynolds-number homogeneous and isotropic turbulence in an enclosed flow apparatus with fan agitation. *Meas. Sci. Technol.* **27** (3), 035305.

Falkovich, G. & Pumir, A. 2007 Sling effect in collisions of water droplets in turbulent clouds. *J. Atmos. Sci.* **64** (12), 4497–4505.

Falkovich, G., Fouxon, A. & Stepanov, M. 2002 Acceleration of rain initiation by cloud turbulence. *Nature* **419** (6903), 151–154.

Ireland, P.J., Bragg, A.D. & Collins, L.R. 2016 The effect of Reynolds number on inertial particle dynamics in isotropic turbulence. Part 1. Simulations without gravitational effects. *J. Fluid Mech.* **796**, 617–658.

de Jong, J., Salazar, J.P.L.C., Woodward, S.H., Collins, L.R. & Meng, H. 2010 Measurement of inertial particle clustering and relative velocity statistics in isotropic turbulence using holographic imaging. *Intl J. Multiphase Flow* **36** (4), 324–332.

Kearney, R.V. & Bewley, G.P. 2020 Lagrangian tracking of colliding droplets. *Exp. Fluids* **61** (7), 155.

Larsen, M.L. & Shaw, R. 2018 A method for computing the three-dimensional radial distribution function of cloud particles from holographic images. *Atmos. Meas. Tech.* **11** (7), 4261.

Lu, J. & Shaw, R.A. 2015 Charged particle dynamics in turbulence: theory and direct numerical simulations. *Phys. Fluids* **27** (6), 065111.

Meng, H., Gang, P., Ye, P. & Woodward, S.H. 2004 Holographic particle image velocimetry: from film to digital recording. *Meas. Sci. Technol.* **15** (4), 673.

Moffat, R.J. 1988 Describing the uncertainties in experimental results. *Exp. Therm. Fluid Sci.* **1** (1), 3–17.

Novara, M., Schanz, D., Geisler, R., Gesemann, S., Voss, C. & Schröder, A. 2019 Multi-exposed recordings for 3D Lagrangian particle tracking with multi-pulse shake-the-box. *Exp. Fluids* **60** (3), 44.

READE, W.C. & COLLINS, L.R. 2000 Effect of preferential concentration on turbulent collision rates. *Phys. Fluids* **12** (10), 2530–2540.

ROSA, B., PARISHANI, H., AYALA, O., GRABOWSKI, W.W. & WANG, L.-P. 2013 Kinematic and dynamic collision statistics of cloud droplets from high-resolution simulations. *New J. Phys.* **15** (4), 045032.

SALAZAR, J.P.L.C., DE JONG, J., CAO, L.J., WOODWARD, S.H., MENG, H. & COLLINS, L.R. 2008 Experimental and numerical investigation of inertial particle clustering in isotropic turbulence. *J. Fluid Mech.* **600**, 245–256.

SAW, E.-W., SALAZAR, J.P., COLLINS, L.R. & SHAW, R.A. 2012*a* Spatial clustering of polydisperse inertial particles in turbulence: I. Comparing simulation with theory. *New J. Phys.* **14** (10), 105030.

SAW, E.-W., SHAW, R.A., SALAZAR, J.P. & COLLINS, L.R. 2012*b* Spatial clustering of polydisperse inertial particles in turbulence: II. Comparing simulation with experiment. *New J. Phys.* **14** (10), 105031.

SAW, E.-W., BEWLEY, G.P., BODENSCHATZ, E., RAY, S.S. & BEC, J. 2014 Extreme fluctuations of the relative velocities between droplets in turbulent airflow. *Phys. Fluids (1994-present)* **26** (11), 111702.

SCHANZ, D., GESEMANN, S., SCHRÖDER, A., WIENEKE, B. & NOVARA, M. 2012 Non-uniform optical transfer functions in particle imaging: calibration and application to tomographic reconstruction. *Meas. Sci. Technol.* **24** (2), 024009.

SCHANZ, D., GESEMANN, S. & SCHRÖDER, A. 2016 Shake-the-box: Lagrangian particle tracking at high particle image densities. *Exp. Fluids* **57** (5), 70.

SELLAPPAN, P., ALVI, F.S. & CATTAFESTA, L.N. 2020 Lagrangian and Eulerian measurements in high-speed jets using multi-pulse shake-the-box and fine scale reconstruction (vic#). *Exp. Fluids* **61** (7), 1–17.

SHAW, R.A. 2003 Particle-turbulence interations in atmospheric clouds. *Annu. Rev. Fluid Mech.* **35** (1), 183–227.

SQUIRES, K.D. & EATON, J.K. 1991 Preferential concentration of particles by turbulence. *Phys. Fluids* A **3** (5), 1169–1178.

SUNDARAM, S. & COLLINS, L.R. 1997 Collision statistics in an isotropic particle-laden turbulent suspension. 1. Direct numerical simulations. *J. Fluid Mech.* **335**, 75–109.

TAVOULARIS, S., BENNETT, J. & CORRSIN, S. 1978 Velocity-derivative skewness in small Reynolds number, nearly isotropic turbulence. *J. Fluid Mech.* **88** (1), 63–69.

WANG, L.-P., WEXLER, A.S. & ZHOU, Y. 2000 Statistical mechanical description and modelling of turbulent collision of inertial particles. *J. Fluid Mech.* **415**, 117–153.

WANG, L.-P., AYALA, O., KASPRZAK, S.E. & GRABOWSKI, W.W. 2005 Theoretical formulation of collision rate and collision efficiency of hydrodynamically interacting cloud droplets in turbulent atmosphere. *J. Atmos. Sci.* **62** (7), 2433–2450.

WANG, L.-P., AYALA, O., ROSA, B. & GRABOWSKI, W.W. 2008 Turbulent collision efficiency of heavy particles relevant to cloud droplets. *New J. Phys.* **10** (7), 075013.

WIENEKE, B. 2008 Volume self-calibration for 3D particle image velocimetry. *Exp. Fluids* **45** (4), 549–556.

YAVUZ, M.A., KUNNEN, R.P.J., VAN HEIJST, G.J.F. & CLERCX, H.J.H. 2018 Extreme small-scale clustering of droplets in turbulence driven by hydrodynamic interactions. *Phys. Rev. Lett.* **120** (24), 244504.

ZHOU, Y., WEXLER, A.S. & WANG, L.-P. 2001 Modelling turbulent collision of bidisperse inertial particles. *J. Fluid Mech.* **433**, 77.